A low-binder-content ink system for 3D printing high-density and small feature size 316L stainless steel parts

*Hao Guo, Jing Qin, Shiyu Zhou, Bo Qian *, Lingying Li, Dezhi Zhu, Xuejun Shi*

Hao Guo, Bo Qian, Lingying Li

Key Laboratory of Multifunctional Nanomaterials and Smart Systems, Suzhou Institute of Nano-Tech and Nano-Bionics, Chinese Academy of Sciences, Suzhou 215123, China;

Jing Qin, Shiyu Zhou

School of Nano Technology and Nano Bionics, University of Science and Technology of China, Suzhou 215123, China;

Dezhi Zhu

Guangdong Key Laboratory for Advanced Metallic Materials processing, School of Mechanical and Automotive Engineering, South China University of Technology, Guangzhou 510640, China

Xuejun Shi

School of Physical Science and Technology, Soochow University, Suzhou 215006, China;

* Corresponding author. E-mail addresses: bqian2010@sinano.ac.cn

Keywords: Binder Jet 3D Printing; Ultralow-binder-content ink system; High density; Small feature size; 316L stainless steel

Abstract

Binder ink system is the backbone of binder jet 3D printing (BJ-3DP) technology. Comparing with metal injection molding (MIM), BJ-3DP needs much less amount of binder, which means less exhaust gas generation during the debinding process and more environmental-friendly. More than that, low content of binder is also supposed to benefit to the structure properties of the printed metal parts. In this paper, an ultralow-binder-content ethanol-water-PVP ink system was demonstrated for the BJ-3DP 316L stainless steel parts by applying thermal bubble inkjet technology. The PVP binder concentration is as low as 80 mg/ml, which

can achieve an ultralow solid content of 0.2 wt% in the printed green part. The two-component solution with water and ethanol provides not only the rheology property adjustment freedom for the ink jetting and infiltration in the metal powders, but also the two boiling points for the step-by-step capillary bridge formation process. By applying the low-binder-content ink, the fully densified 316L stainless steel parts after sintering can obtain the relative density up to 99.4%, Vickers hardness up to 185 HV, tensile strength up to 542 MPa, 25% elongation at break, and feature size as small as 200 μm.

1.Introduction

Additive manufacturing (AM) or 3D printing is fundamentally changing the way of parts production. Different from typical manufacturing by cutting away or molding material, 3D printing layer by layer builds up complex, three-dimensional products guided by digital designs, with largely reduced material waste [1]. Many printable materials have been developed for 3D printing, including metal [2], polymer [3], ceramics [4] and concrete [5]. Among these materials, 3D printing metal is showing excellent perspectives of growth due to high demand arising prominently from the healthcare [6], automotive [7], aerospace [8] and defense [9] sectors. At the same time, 3D printing metal technology like powder bed fusion, binder jet 3D printing (BJ-3DP), and directed energy deposition have grown at an explosive pace [2]. Among these technologies, BJ-3DP attracts more and more attentions since it is the fastest and cheaper metal 3D printing technology, without support structure, and keeps low temperature during printing [10]. BJ-3DP is similar with metal injection molding (MIM) for using the similar metal powders and sintering process [11]. However, the green parts formation processes are fundamentally different for BJ-3DP and MIM. Usually, for injection lubrication, 5-10 wt% binder is mixed with metal powders by blender for MIM, which will generate a large amount of exhaust gas during debinding process [12]. The MIM green parts are prepared by injecting the powder-binder mixture into a mold. On the contrary, BJ-3DP doesn't need high content binder since the thin metal powder layers are dispensed separately, which means less debinding time and exhaust gas, and more environment friendly [13]. After the binder ink being jetted following the design sliced pattern layer by layer, infiltrating in the metal powder, and being cured, the BJ-3DP

green parts can be obtained.

The underlying mechanism of the lower content binder requirement of BJ-3DP comparing with MIM is basically similar with the stiffness of a wet granular pile bestowed by the liquid surface tension induced Laplace pressure in capillary bridges [14]. The only difference is the BJ-3DP binder is solid at room temperature, and will be soften by thermal curing [15]. Due to the rheology requirement of inkjet printing, the binder had to be carried by large amount solvents. After the solvents being evaporated, the small amount binder was left between particles and played a role which can be analog as liquid capillary bridges in a wet granular pile. Since the volume of the liquid capillary bridges can be very small, the binder amount can also be very small.

There are two kinds of inkjet technology usually used in 3D printing, one is piezoelectric inkjet (PIJ), the other is thermal-bubble inkjet (TIJ) [16]. PIJ usually requires higher ink viscosity (>10 cP) than TIJ (<5 cP) [17], which means TIJ has bigger chance to achieve lower binder content. In this paper, we try to use TIJ to study BJ-3DP of metals with low binder content. Water was used as one of the main solvents in the binder ink, which is the most popular solvent for bubble generation in TIJ [18]. As a kind of non-toxic, non-polluting water-soluble polymer, polyvinylpyrrolidone (PVP) was selected as the binder [19]. Considering the high surface tension and boiling point of water, large amount ethanol was added into the ink to tune the surface tension for better jetting performance and infiltration effect, and provide lower boiling point for fast evaporation to form capillary bridges during printing [20]. To avoid excess substances left in the final printed metal parts, the ethanol-water-PVP ink system is simple without any surfactants or stabilizers.

After inkjet 3D printing and thermal curing, the capillary bridges step-by-step formed in the printed green part due to the two different boiling points of water and ethanol. We suggest that such step-by-step capillary bridges formation process will contribute to the densification of the printed structures. After the solvents were all evaporated, the PVP binder were left in the green part and inherited the shape of liquid capillary bridges between the metal particles. During sintering, binder is supposed be softened to a quasi-liquid state at the beginning to play a role similar with liquid capillary bridges to retract the particles close to each other. At the same time, less binder will ensure closer distance between metal particles, and fewer bubbles and carbon

residues generation. These will also contribute the densification of the final structures. Additionally, the fast evaporation of ethanol by infrared drying during printing can efficiently control the ink infiltration between the metal particles, and will be helpful to reduce the feature size of the printed structure.

Using the low-binder-content ink, we successfully printed 316L stainless steel parts with the relative density up to 99.4%, Vickers hardness up to 185 HV, tensile strength up to 542 MPa, 25% elongation at break, and feature size as small as 200 μm. The ink jetting and ink-particle interaction mechanisms were carefully studied by simulation and experiment. The structure properties by sintering with different temperatures were also carefully studied in this paper.

2. Results and analysis

2.1. Printing process analysis

The jetting frequency dependent droplet flight images are shown in Figure 1a. Note that the images were captured at the same delay time. In Figure 1a, all the droplet flight images exhibit main drops and satellite drops. With the increase of frequency, the distance between main drop and nozzle plane increases, which indicates the drop flight velocity increases; the drop volume decreases, and the amount of satellite points increases, which means that the droplet instability increases. After reaching 2.5 kHz, the main drop is hard to be distinguished, which means the volume of main drop has decreased to a value comparable with satellite drop. The frequency dependent main drop volume and velocity curves are shown in Figure 1b. According to Figure 1b, we chose the frequency at the middle point of the flat part of the curves, 1 kHz, as the 3D printing frequency. In details, we measured the ink viscosity at different shear rates in Figure 1c. The ink viscosity shows no big change with the increase of shear rate, which means PVP molecular chains have no entangled with each other in the ink and is consistent with the characteristics of dilute polymer solution. We simulated the process of ink ejecting from the nozzle using the surface tension and viscosity of the ink in Figure 1d. It can be observed that the satellite drops are mainly generated from the droplet tail after broken from the nozzle. Usually, the jetting performance of inkjet droplet can be characterized by three dimensionless physical constants including Reynolds number (Re), Weber number (We) and Ohnesorge number (Oh) [21]:

$$Re = \frac{v\rho a}{\eta} \tag{1}$$

$$We = \frac{v^2 \rho a}{\gamma} \tag{2}$$

$$Oh = \frac{\sqrt{We}}{\mathrm{Re}} = \frac{\eta}{(\gamma \rho a)^{1/2}} \tag{3}$$

Where v is the jetting drop velocity (m/s), ρ is the ink density (g/mL), a is the nozzle diameter (μm), η is the ink viscosity (mPa·s), γ is the surface tension (mN/m). If the inverse of the Ohnesorge number $Z=1/Oh$ is in the range of $10 > Z > 1$, the ink is printable and usually with stable jetting performance. At the print frequency of 1kHz, Z was calculated of 7.8, which is in the stable jetting range.

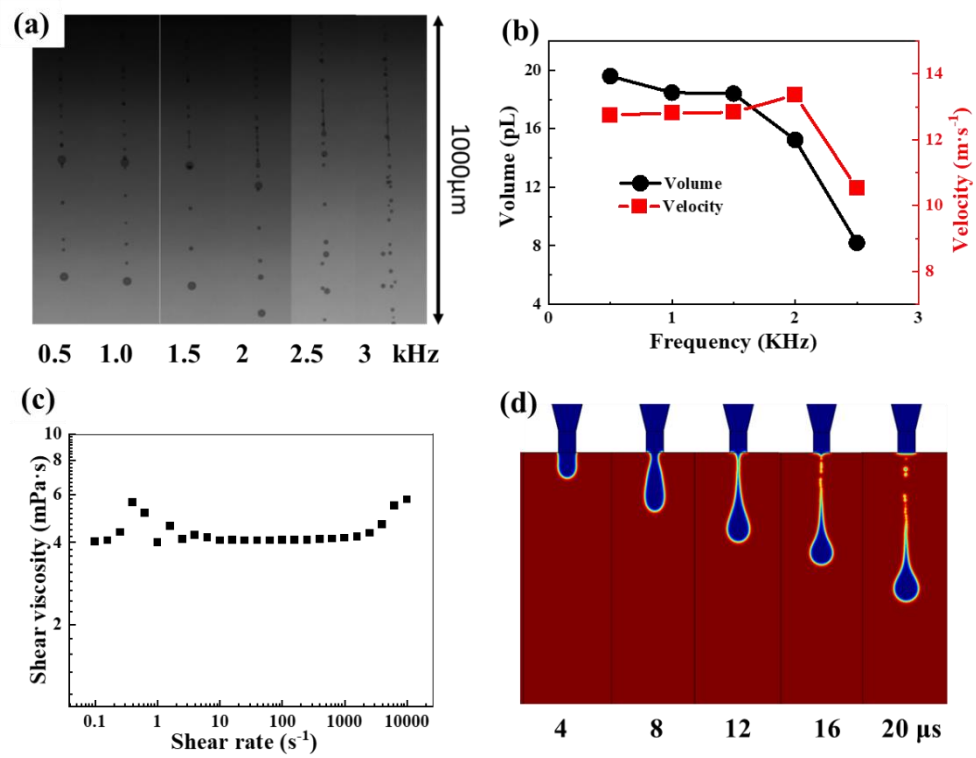

Figure 1. Droplet jetting properties. Frequency dependent (a) droplet flight images; (b) droplet volume and velocity; (c) Ink viscosity at different shear rate; (d) Inkjet droplet process simulation.

Based on the stable jetting, it is important to study the drop impact and infiltration mechanisms on and between the powder particles for BJ-3DP. Because real-time observation of droplet behavior in powder bed is very complex and difficult[22], the mechanisms was studied by simulation. We simplified the model with fixed particle arrays and only studied the fluid

behavior of inkjet droplet as shown in Figure 2. The upper images in Figure 2a show the impact and infiltration events of the first droplet. After hitting on the particle arrays, the droplet spreads along the particle surface to a width of three particles and penetrates from the first particle layer to the second layer. The bottom images in Figure 2a are the fluid velocity contours. Note that the fluid includes the surrounding air and drop liquid. The drop impacts the air on and surrounding the flight trace like a bullet by pushing and scratching, which make the velocity of the impacted air increased. When the drop hits on a particle, the splashing action of the drop can be observed, the surrounding air is also impacted by the splashing liquid. Then, the liquid penetrated into the particle arrays with a rather high velocity. After that, the liquid velocity is quickly decreased to close to zero due to the flow resistance between the particles, with the impacted air still flowing by inertial force. In the upper second drop events images in Figure 2b, it can be observed that there is a satellite drop at the left side of the main drop. The second drop spreading and infiltration events are similar with the first one. The merge of liquids of the first and second drop in particle arrays is good and spreads to a width of 4 particle size and a depth of 2 layers. Note that the nozzle position has been moved laterally with a drop size distance when jetting the second drop. The lower images of fluid velocity contours in Figure 2b shows some differences from that in Figure 2a. The second drop velocity is obvious faster than that of the first one. The fluid velocity distribution along and around the drop flight trace is asymmetric, which is also different from the symmetric distribution in Figure S2a. We suggest the second drop flight is disturbed by the remained air flow impacted by the first one. Due to the impact air flow with a direction downward to the particle arrays, the flow resistance for the second drop is lower than that for the first one, which results in a faster drop velocity. Also due to the air flow impacted by the first drop, the air along and around the second drop flight trace tends to flow to the flight trace of the first one, which makes the fluid velocity distribution asymmetric, and the satellite drop turn to the left of the main drop. When the 6th drop approaching to the particle arrays as shown in the first image in Figure 2c, the liquid of the previous drops has fast spread to a width of 10 particle size and a height of 3 layers, with small part of the liquid spilled over the surface of the particle array, and some small empties between the liquid infiltrated particles. The spread width of previous drops has already larger with about 3 particle width than the nozzle lateral movement distance for the 6th drop. After

several 5ms intervals as shown in the other images in Figure 2c, the previous drop spread width continues to increases, with the distance difference between the approaching drop and the right edge of spread liquid increasing from 3 particle to 4 particle width. The downward air flow impacted by the flight drop makes the spilled liquid sunken under the approaching drop. After the drop jetting is stopped as shown in Figure 2d, the spilled liquid on the surface of the particle arrays disappears with the liquid fully infiltrating between the particles only in 1s. The final infiltration depth changes from 3 to 4 particle layers. The cross-section of infiltration morphology is generally inverted trapezoid, with the right edge of 3 particle layers depth and 4 or 5 particle width. The results in Figure 2 demonstrate the fast and good ink infiltration effect between the particles, except the printed structure edge is not just the landing position of the final drop but with several particle distance out of the designed edge. This lateral spread of ink is unavoidable by capillary force due to the low surface tension ink designed for fast and good infiltration. Note that such small-scale liquid spread behavior will not have big influence on the final structure due to the large-scale shrinkage during sintering. The inverted trapezoid cross-section morphology is the origin of the surface roughness of the final structures.

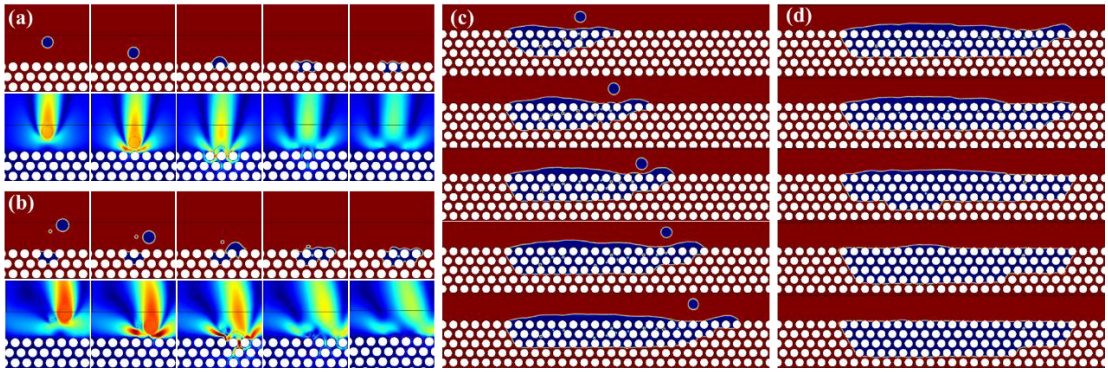

Figure 2. Process simulation of the (a) first droplet and (b) second droplet impinging on the powder bed, 5μs interval per picture; (c) Process simulation of ink droplet impinging on the powder bed, 5ms interval per picture; (d) Simulation of ink diffusion in powder, 20ms interval per picture.

After the ink jetted on the powder bed, the infrared lamp will open to heat the printed pattern. Since the drops infiltration is very fast, when the infrared light opened, the drops has fully infiltrated between the particle arrays. Note that on-line infrared light heating is necessary to

increase the strength of the printed structure to bear the shear force induced by the powder spreading. To directly observe the occurrences during infrared heating, we designed a separate experiment. 0.1wt% DCM dye molecules (DCM, 4-(Dicyanomethylene)-2-methyl-6-(4-dimethylaminostyryl)-4H-pyran, purchased from Aladdin) was added into the ink, and printed on the powder with one layer thickness. Then, the printed powder was quickly heated by an infrared lamp to about 60°C, which was measured by a thermometer and same with the temperature during 3D printing. At the same time, the printed powder pattern was excited by 350 nm ultraviolet (UV) light. Due to the existence of DCM dye, the liquid morphology between particles can be easily distinguished as shown in Figure 3a-c. Under the excitation of UV light, the metal particle exhibits purple color, the liquid between particles shows red color. With the infrared light heating time increasing, the red color of liquid becomes clearer and clearer. Finally, clear capillary bridges with red color between the particles can be observed in Figure 3c. The capillary bridges efficiently strengthened the printed pattern as a wet granular pile, which was strong enough to be not destroyed by powder spreading during 3D printing.

To further understand the evaporation effect of ink on the surface of stainless-steel particle, we studied the evaporation process under infrared light irradiation by dripping drops with four different components of the ink on a 316L polished metal plate. The components of Droplet in Figure 3d-g were PVP+ethanol, water+ethanol, PVP+water+ethanol (the 3D printing ink itself), and PVP+water, respectively. Note that the ratios of different components of the droplets were same with that in the 3D printing ink. The volumes of the droplets were also same. It can be observed that PVP+ethanol droplet was the fastest dried drop, which was completely evaporated to coffee ring in only 100s. The second was water + ethanol droplet, which was dried at about 460s. Then, the 3D printing ink was dried at 600s. The slowest was PVP+water droplet, which used about 780s to be dried. The results demonstrate that ethanol can be quickly evaporated. Comparing the evaporation time between PVP+ethanol and PVP+water droplets, the dried time of water is about 6 times slower than that of ethanol, which made the 3D printing ink not only the fast infiltrate between the particles due to the existence of ethanol with low surface tension, but also quickly stop the infiltration due to the fast evaporation of ethanol. Comparing between water+ethanol, the 3D printing ink, and PVP+ethanol droplets, it can be observed that the existence of PVP can make the residual after evaporation more uniform than

that without PVP [23]. The coffee ring of PVP+ethanol droplets after evaporation is larger with blurrier edge than that of the 3D printing ink, and PVP+water droplets, which means the existence of water can make the residual PVP denser due to high surface tension. The results indicate the residual PVP between the particles will be dense and inherit the morphology of liquid capillary bridges, which will benefit to strengthen the green part.

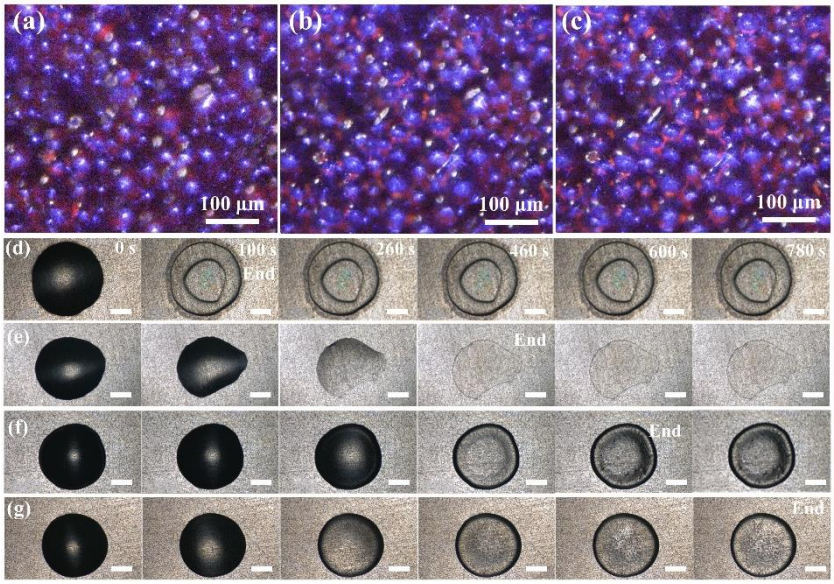

Figure 3. (a-c) Drying process of ink in powder, 15s interval per picture; Droplet evaporation morphology of different components of ink on a polished stainless steel plate (d) PVP+ethanol, (e) water+ ethanol, (f) PVP+water+ethanol, and (g) PVP+water.

2.2. The morphology of green parts

The printed green parts are shown in Figure 4 a-b. It can be observed that the outline of the printed green parts is clearly defined. Figure 4c-d show the SEM images of the microscopic surface morphology of the green parts. It can be observed that the metal particles are tightly assembled by the capillary bridge-like binder connections. The mean distance between the metal particles is very small, which means the amount ratio of the binder in the green part is very low. To evaluate the amount of binder, we firstly calculated the volume ratio τ of the ink in the green part according to the formula 4:

$$\tau = \frac{n \cdot v \cdot r \cdot b}{V \cdot h \cdot 1000 \cdot 25400} \quad (4)$$

Where, τ is the volume ratio of ink and green part, n is the print frequency (Hz); v is the volume of ink droplet (pL); r is one-pass print resolution (DPI); b is the number of printing times; V is the moving speed of print head (mm/s); h is the thickness of the powder layer (mm).

Note that r is 75 DPI. According to the parameters in Table S2, τ was calculated as 53%. Since the binder concentration in the ink is 8 g/100 mL, the mass ratio of binder in green part is only about 0.2 wt%.

To explore the feature size limit of our printed parts, two micro-frames with structure period of 2mm and 1mm, respectively. The 2mm period sample has grid rib and square pore sizes of 0.8 mm and 1.2 mm in Figure 4e, respectively. The 1mm period sample has 0.3 mm grid rib and 0.7 mm pore, respectively, as shown in Figure 4f-g. It can be observed that the two micro-frames can be clearly defined by BJ-3DP. Since the particle size is about 41.43 μm, the small grid rib size of 300 μm of 1mm period sample is about 7 particle size, which is about five droplets printing and spreading size in lateral direction if deduced from simulation results in Figure 2a-b. The results indicate the droplet infiltration can be efficiently controlled, and the small amount and capillary bridge-like PVP binder connection was strong enough, which both contributed to realize such small grid rib size. The compressive strength of the printed green body at different direction is tested as shown in Figure S4. The maximum compressive strength reached 2.5 MPa, which could meet the printing requirements for precision parts of general size [24].

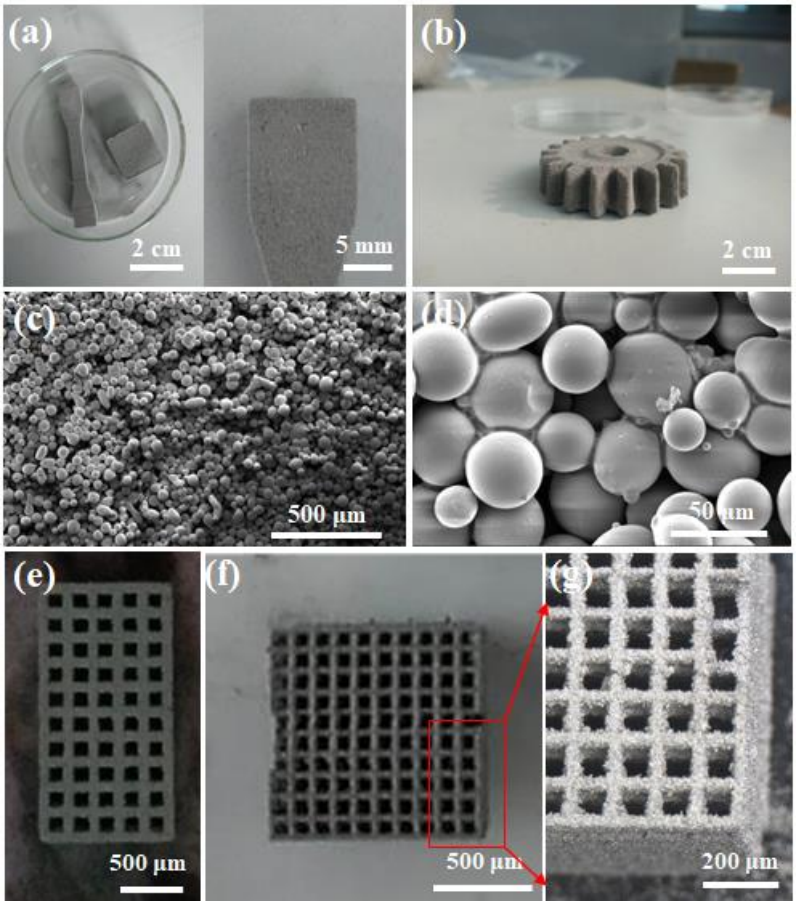

Figure 4. 3D printed green parts: (a) Spline and square; (b) Gear; (c, d) surface micromorphology; (e-g) Micro-frames.

2.3. Micro-structure of sintered sample

Low binder content in the green part will significantly reduce the debinding time as shown in Figure S3c. After debinding, to explore the best sintering condition, the sintering temperature was varied from 1250 °C to 1290 °C, with the SEM images of polished sample surfaces shown in Figure 5b-f, respectively. Note that the SEM surface morphology image of green part is shown in Figure 5a as a reference. It can be observed that the microstructure evolution after sintering can be divided to three stages. The first stage is from 1250 °C to 1270 °C, during which the sintering neck gradually grew until the spaces between the metal particles were completely filled with the temperature increasing. The micro-grain structures can be distinguished, but are not clear since the grain boundaries are blurry, and the micro-grains themselves are not pure with many black points. The second stage is from 1270 °C to 1280 °C, during which the elements in the sintered sample redistributed, and the micro-grain structures

are clearly separated. The number of black points in the grains is significantly reduced. The third stage is from 1280 °C to 1290 °C, during which the size of micro-grains grew with the temperature increasing. The number of black points in grains continues to decrease. The densities of the sintered samples with temperature from 1250 °C to 1290 °C were measured by a densimeter as 7.12, 7.45, 7.81, 7.93, and 7.95 g/cm^3, respectively. Since the true density of 316L sintered parts is 7.98 g/cm3, the relative density can reach 99.4% when the sintering temperature is 1280 °C. Note that the shape of samples sintered at 1290 °C was distorted. Thus, 1280 °C is the optimized sintering temperature.

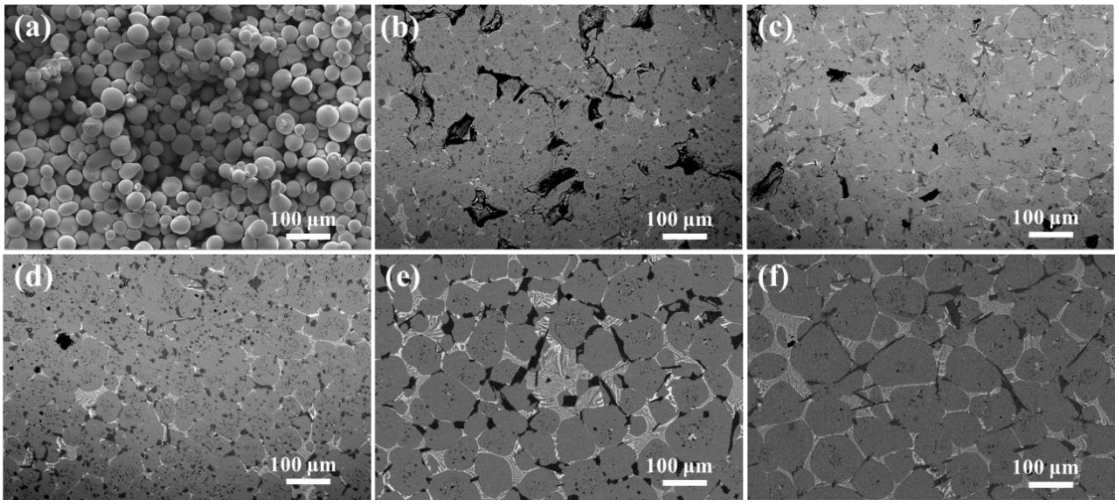

Figure 5. (a) SEM image of green part surface topography. Backscattering electron imaging of polished (b) 1250°C, (c)1260°C, (d)1270°C, (e)1280°C, (f)1290°C sintered samples.

To better understand the sintering mechanism, energy dispersive spectroscopy was used to measure the element distribution in the SEM backscattering electron images of the sample sintered at 1280 °C as shown in Figure 6. Table 1 shows the measured element weight percent at the six points in Figure 5. According to the results of Table 1, the micro-grains are austenite formed by Fe-Cr-Ni-C (γ-Fe) solid solution (point 1) [25]; the dark parts (point 2 and 4) between the micro-grains are ferrite precipitated during the solidification process (cooling process after sintering) [26]. It is obvious that the ferrite mainly concentrated at the edge of the austenite, and only a small amount of ferrite exists inside the austenite (point 3). The existence of ferrite can improve the strength of 316L stainless steel, but will reduce the toughness of stainless steel. The white strips (point 5) at the grain boundary are the sigma phase formed by Mo and Cr

elements [27]. The strip morphology is due to the low melting point of Mo element induced capillary force driven flow between the micro-grains during sintering.

In this case, the capillary forces generated during sintering are the main driven forces for the structure densification, which include the sintering neck capillary bridge force retracting the metal particles close to each other, and the low melting point element like Mo filling the channel between the metal grains by capillary force. Due to the melting point difference between different elements, the different capillary force driven actions dominated at different temperatures, as shown in Figure 5b-f. Note that the capillary-bridge-like PVP binders in the green part can also retract the metal particles close to each other during the heating period from room temperature to the debinding temperature, with the binders being soften to act as liquid capillary bridges. Attributed to the low amount of binder, the original distances between metal particles in green part are very close as shown in Figure 4d, which will also benefit to the final densification of the metal structure. Since EDS is not a particularly sensitive technology in general, it cannot precisely detect the proportion of trace elements and elements with low atomic numbers, so its measurement of C and O elements is inaccurate [28]. So, sulfur carbon analyzer and nitrogen oxygen analyzer were used to measure the elements of the sintered sample (1270 °C). The proportion of C element is 0.075%, and the proportion of O element is 0.0075%, which are significantly lower than the element ratios of C and O in the green part. Therefore, it can be considered that most of the binder during the sintering process has been removed completely, but there are still some residues that cannot be removed and diffuse into the austenite and ferrite grains.

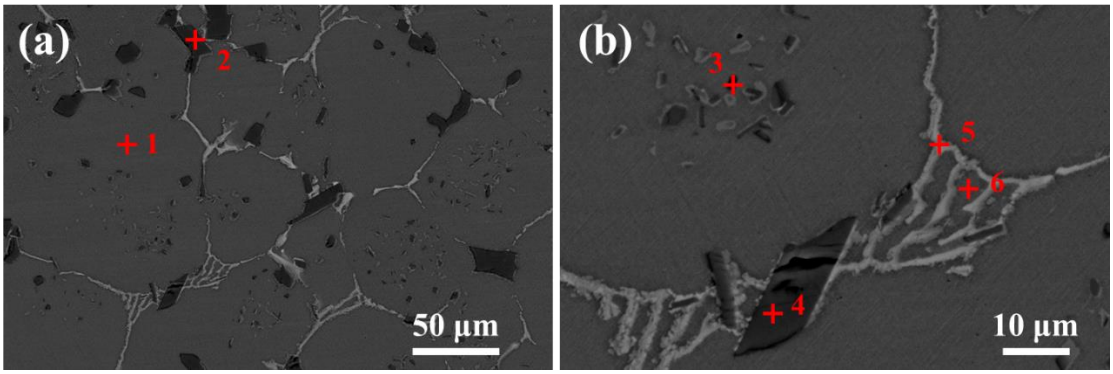

Figure 6. Backscattering Electron Imaging of Sintered Samples.

Table 1. EDS Element Analysis

Wt%	C	Si	Cr	Mn	Fe	Ni	Nb	Mo
1	2.17	1.55	15.94	0.00	62.85	11.81	0.39	5.28
2	4.51	0.35	56.96	0.00	30.75	0.73	0.14	6.57
3	3.51	0.66	41.32	0.11	41.91	3.96	3.73	4.8
4	4.34	0.63	55.08	0.21	29.00	0.91	4.09	5.74
5	4.19	0.54	19.97	0.17	35.75	5.58	13.2	20.6
6	1.48	1.46	14.95	0.20	61.35	11.93	2.95	5.69

2.4. Chemical composition analysis

Figure 7 shows the XRD patterns of printed samples sintered at different temperatures. It can be observed that the sintered sample contains two phases, γ-austenite (γ-Fe) and δ-ferrite (δ-Fe) phase which is consistent with EDS elemental analysis [29]. During the sintering process, the austenite promoting elements (usually Ni and C) diffusion in γ-Fe matrix, ferrite promoting elements (usually Cr and Mo) diffusion at the grain borders. The peak positions remain basically same at different sintering temperature. The intensity of the main diffraction peak at 44° reaches maximum when the sintering temperature is 1270°C, which are consistent with the element redistribution and grain growth processes as shown in Figure 5b-f.

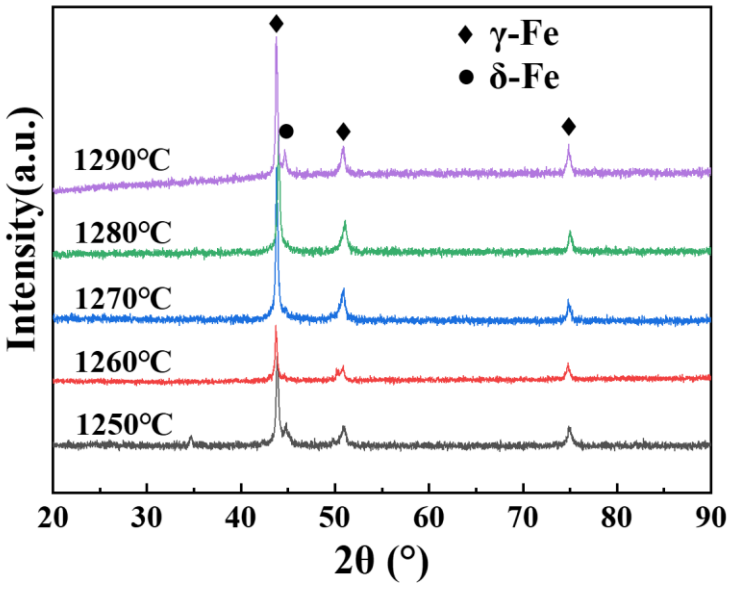

Figure 7. X-ray diffraction patterns of printed 316 L stainless steel samples at different sintering temperatures.

2.5. Effect of sintering temperature on microstructure

Figure 8 shows the photos and SEM images of the BJ-3DP micro-frame samples after sintered at 1280 °C. The mechanical spine shows 20% linear shrinkage after sintering the which is same for the frame structure. Figure 8b-c confirms the grid ribs and pores maintain the design shape after sintering.

The micro-frames structure details were imaged by SEM in Figure 8d-i. It can be measured from Figure 8d-e, the periods of two micro-frame samples in Figure 4e-f shrink to about 1.59 mm and 0.78 mm periods, respectively. The grid rib and pore sizes of the micro-frames in Figure 8d-e are about 0.65 mm and 0.94 mm, and 0.2 mm and 0.58 mm, respectively. The surface of the samples in Figure 8d-e are a little bit rough due to the fusion and aggregation of metal particles during sintering. The micro-frame samples were polished and measured by SEM secondary electron images in Figure 8f-g. It can be observed that the internal structure of the frame grid ribs is dense without any holes. Figure 8h-i are the SEM backscattered electron images of the polished micro-frame samples, in which the austenite grain morphology after sintering is similar with that in Figure 5e. The size of the grains are in the range of 50 ~ 100 μm. The results indicate that the final structure dimension and quality are controllable if considering the sintering induced shrinkage. The minimum feature size of 200 μm can be realized for the designed 1mm period micro-frame sample.

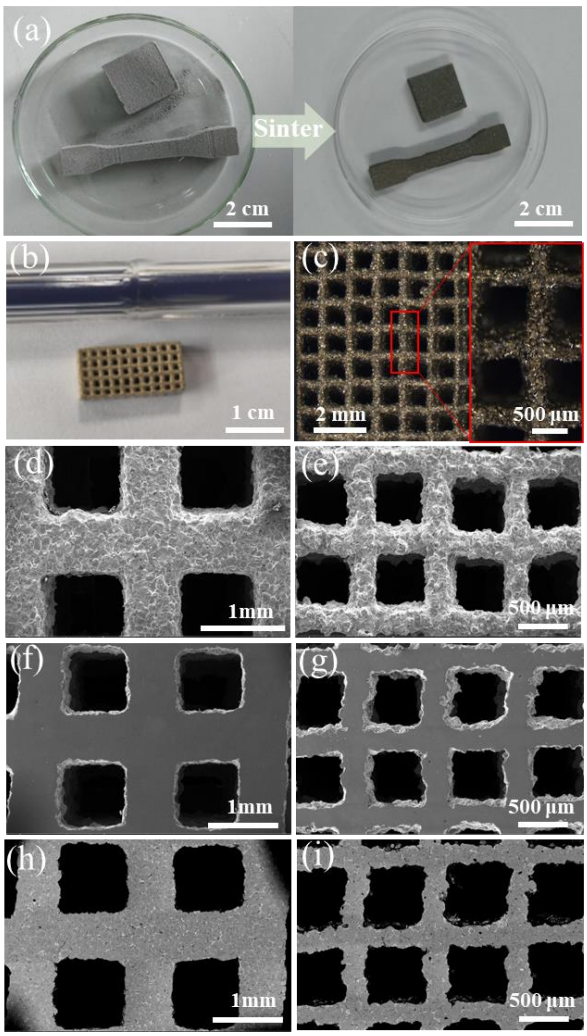

Figure 8. The digital photos of designed (a) tensile sample, (b) 2mm and (c) 1 mm period micro-frames after sintering; The SEM (d-e) surface morphology, (f-g) secondary electron, and (h-i) backscattering electron images of the designed 2mm and 1 mm period micro-frames, respectively.

2.6. Mechanical properties

Figure 9a presents the hardness of the samples sintered at different temperatures. The hardness increases with the sintering temperature increasing, and reaches a maximum Vickers hardness of 190.5 HV at 1280 °C, then shows a little bit decreases at 1290 °C. This is due to the porosity decreasing with sintering temperature increasing as shown in Figure 5b-e. When the sintering temperature achieves the super solidus liquid sintering temperature point, the hardness increases rapidly with the enhancement of sample density. When the temperature exceeds 1290°C, Mo accumulates at the austenite grain boundary with ferrite decreasing, which resulting in the decrease of hardness.

Figure 9b illustrates the tensile properties of the printed 316L parts dependent on the sintering temperatures. It is obvious that the tensile properties of the parts sintered at 1260°C are bad, then are improved with sintering temperature increasing from 1260 °C to 1280 °C, and achieve a maximum tensile strength up to 536 MPa at 1280°C, and maximum elongation at break up to 25%, which is dependent on the porosity of the samples as shown in Figure 5b-e according to the formula proposed by by Salak et al. [30]

$$\frac{\alpha}{\beta} = exp\ (4.3\gamma) \tag{5}$$

where α is the tensile strength of the sintered material, β is the tensile strength of the fully densified material and γ is the porosity of the sintered material, the higher the densification degree of sintered parts, the stronger the mechanical strength. The tensile strength and elongation at break of the sample at 1290°C show a little bit decrease, which is due to the growth of austenite grain and the large aggregation of Mo at austenite grain boundary as shown in Figure 5f.

Figure 9c-d are the SEM images of the tensile fracture of the part sintered at 1290°C. Some big and small dimples on the tensile fracture surface of the sintered sample in Figure 9c-d can be observed, with the size of about 50 μm and 1 μm, which indicates that the fracture mode of the tensile sample is a mixture of ductile brittle and transgranular fractures. Comparing with the big dimples, the small dimples are deeper with a larger proportion and larger plastic deformation. It can be observed that there are tearing edges on the extension fracture, which will increase the plastic deformation, consume energy, the resistance during crack propagation, and the tensile strength.

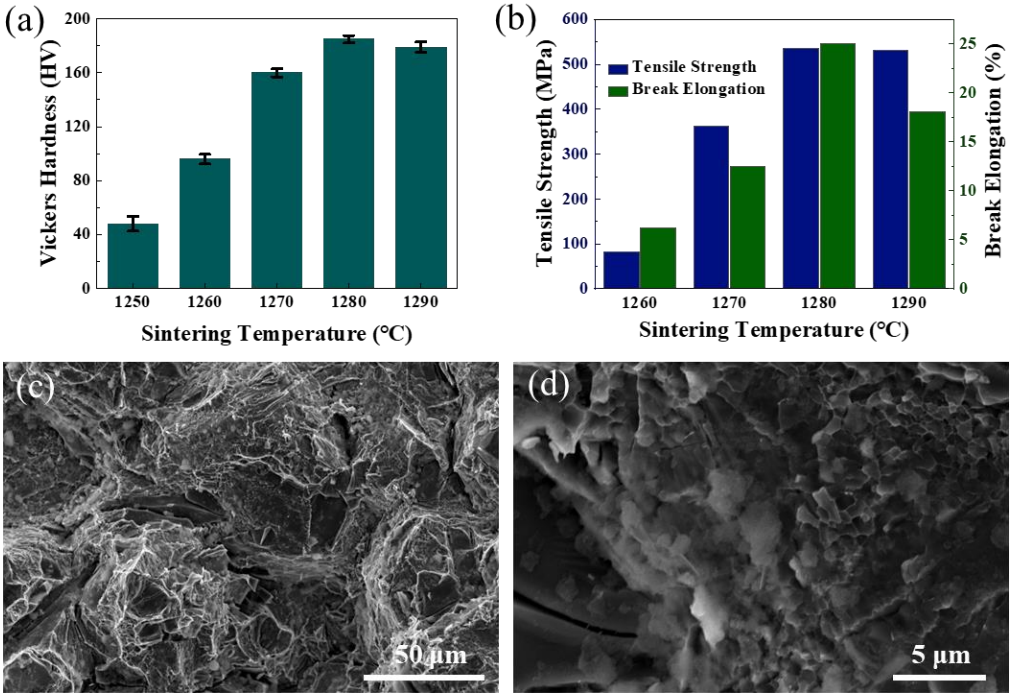

Figure 9. (a) Hardness of samples sintered at different temperatures; (b) Tensile properties of 316L stainless steel sintered parts;(c-d) Tensile Fracture Morphology of 316L Sintered Parts.

3. Conclusion

We applied thermal inkjet technology to reduce the binder amount during BJ-3DP 316L stainless steel parts. According to the simulation and experiment, the ethanol-water-PVP ink system was demonstrated to infiltration controllable with even ink distribution between the metal particles and without over spread out of the boundaries of the design pattern. Benefit from the step-by-step capillary bridge formation processes with the low content binder and optimized sintering conditions, after being sintered at 1280 °C, the relative density of 316L stainless steel reached up to 99.4%, with the mechanical properties of Vickers hardness of up to 190.5 HV, tensile strength of 536 MPa and elongation at break of 20%. After sintering, austenite micro-grains can be observed and formed by Fe-Cr-Ni-C solid solution (γ-Fe), while ferrite distributed between the austenite micro-grains with the sigma phase formed by Mo and Cr stripes. Mo and Cr at the grain boundaries can reduce the sintering activation energy and benefit to the densification of the structure. The tensile properties and hardness of the samples increase rapidly with the raise of structure density, with the mixed brittle and transgranular tensile fractures. We designed and printed 2mm and 1mm period 316L stainless steel micro-frames. After sintering at 1280 °C, the micro-frame shrinks uniformly and controllable, with

the minimum feature size of grid ribs achieves to 200 μm. The grid ribs of the frame are dense without holes. The austenite grains of the micro-frames after sintering have the similar shape and size with the bulk structures.

4. Experimental Section

Metal powder: 316L stainless steel gas atomized powder (purchased by Nangong Kejin Welding Materials Co., Ltd) was used in the experiment. The measured chemical components of 316L stainless-steel powder by energy dispersive spectroscope (EDS) are shown in Table S1, which are confirmed in the range of standard. According to the size distribution in Figure S1a, the volume weighted mean diameter (D) of the metal particles was calculated as 41.430 μm. In the SEM image in Figure S1b, the particles show smooth surface and good sphericity. According to ASTMB212-17, the measured bulk density of 316L powder is 4.45 g/cm^3.

Design of ink: To reduce the binder amount, the home-made thermal inkjet (TIJ) printhead was used due to the jetting requirement of low viscous ink. 33.3 wt% water was used as one of the solvents for stable bubble generation of TIJ. However, water has high surface tension. To reduce the surface tension to achieve good jetting condition and fast infiltration between metal particles, 66.6 wt% low surface tension ethanol was added into the ink. Meanwhile, the lower boiling point of ethanol can be quickly evaporated by infrared drying after fast infiltration process during printing, which will help for the formation of liquid capillary bridges between metal particles and limit the infiltration region. PVP/K17 (Polyvinylpyrrolidone, purchased from Aladdin) was selected as the binder with the concentration of 8 g/100 mL. The ink preparation process is as follows: Dissolve PVP in a mixed solvent of water and ethanol and filter with a 5-micron filter. The surface tension and apparent viscosity of the ink was were measured as 27.3 mN/m and the apparent viscosity was 4.37 mPa·s, respectively.

Printing parameters: The schematics of the home-made binder jetting 3D printer is illustrated in Figure S2a, which is equipped with double powder supply bin, one powder bed, home-made TIJ inkjet printhead, and infrared heating lamp. The TIJ printhead has 16 nozzles, with the nozzle size of 40 μm. As shown in Figure S2a, the 3D printing process with one layer powder can be described as following: the leveling roller spread the one-layer powder from powder supply to powder bed, then the ink was jetted on the powder bed according to the design pattern

as shown in Figure S2b; right after that, the infrared lamp was opened to heat the printed pattern. After repeating the one-layer print process layer by layer, the 3D structure embedded in the powder bed was finished. The printing parameters are shown in Table S2.

Sintering parameters: After printing, the printed 3D structure with the surrounding support powders was transferred to a vacuum drying oven, to dry all the liquid in the structure with 150°C, 2 hours. After that, the printed 3D structure was strengthened only by binder connection between metal particles, which was strong enough to support the next surrounding powder cleaning process. After the printed 3D structure being cleaned, the green part was ready for sintering. To design the sintering curve for the green part, the thermogravimetric (TG) curve of PVP and differential scanning calorimetry (DSC) curve of 316L stainless steel powder were measured as shown in Figure S3a-b. Since most mass of PVP was lost at 600°C in Figure S3a, the degreasing temperature was set at 600°C. In Figure S3b, the melting of 316L stainless steel powder can be observed to begin at about 1200°C. According to the results in Figure S3a-b, we designed the sintering curve as shown in Figure S3c, with the temperature raising to 600°C with 5°C/min, and keeping at 600°C for 30 min to remove the binder, then increasing to the sintering temperature at around 1200°C with a speed of 10°C/min, and holding for 3 hours. Finally, we reduced the temperature with 5°C/min to room temperature. The absolute vacuum during sintering was $1x10^{-3}$ Pa.

Characterization: The surface morphology of the powders, green parts and final sintered stainless-steel parts were photographed by FEI Quanta FEG 250 field emission environment scanning electron microscope with secondary electron mode for the powders and green parts, and back-scattering electron mode for the stainless-steel parts, respectively. The X-ray diffraction spectra were tested by powder X-ray diffractometer (D8 Advance, Bruker, Germany). The proportion of carbon element was determined by sulfur carbon analyzer (CS600-Series, LECO Corporation, United States), and the proportion of oxygen element was determined nitrogen oxygen analyzer(ONH836, LECO Corporation, United States). The particle size distribution of the powder was measured by laser particle size analyzer (Mastersizer 2000, Malvern, UK). TG curves of the binder were measured by thermalgravimetric analyzer (TGA/DSC 3+, mettler Toledo, Switzerland). The bulk density of powder was measured by loose density tester (FBS-1002, matsuhaku, China). The density,

mechanical tensile strength, and hardness of the stainless-steel samples were measured by solid electron densitometer (FK-30, matsuhaku. China), electronic universal testing machine (MTS Exceed E44, MTS, China, and digital display Brinell hardness tester 570HAD, Shaoxing Jingbo Testing Instrument Co., LTD, China), respectively.

Supporting Information

Supporting Information is available from the Wiley Online Library or from the author.

Acknowledgements

The authors gratefully acknowledge financial support by R&D Plan for Key Areas of Guangdong Province (No. 2018B090905002), National Natural Science Foundation of China (No. 61575216), Key R&D programs in Jiangsu (No. BE2017082) and Suzhou Science and Technology Program (No. SYG201850).

Hao Guo and Jing Qin contributed equally to this work.

Reference:

[1] T. D. Ngo, A. Kashani, G. Imbalzano, K. T. Q. Nguyen, D. Hui, Composites Part B-Engineering 2018, 143, 172.

[2] T. DebRoy, H. L. Wei, J. S. Zuback, T. Mukherjee, J. W. Elmer, J. O. Milewski, A. M. Beese, A. Wilson-Heid, A. De, W. Zhang, Progress in Materials Science 2018, 92, 112.

[3] S. C. Ligon, R. Liska, J. Stampfl, M. Gurr, R. Muelhaupt, Chemical Reviews 2017, 117, 10212.

[4] C. Chen, X. Wang, Y. Wang, D. Yang, F. Yao, W. Zhang, B. Wang, G. A. Sewvandi, D. Yang, D. Hu, Advanced Functional Materials 2020, 30.

[5] S. Lim, R. A. Buswell, T. T. Le, S. A. Austin, A. G. F. Gibb, T. Thorpe, Automation in Construction 2012, 21, 262.

[6] A. Awad, F. Fina, A. Goyanes, S. Gaisford, A. W. Basit, Advanced Drug Delivery Reviews 2021, 174, 406.

[7] J. H. Martin, B. D. Yahata, J. M. Hundley, J. A. Mayer, T. A. Schaedler, T. M. Pollock, Nature 2017, 549, 365.

[8] B. O. Omiyale, T. O. Olugbade, T. E. Abioye, P. K. Farayibi, Materials Science and Technology 2022, 38, 391.

[9] C. Huang, G. Q. Jian, J. B. DeLisio, H. Y. Wang, M. R. Zachariah, Advanced Engineering Materials 2015, 17, 95.

[10] A. Mostafaei, A. M. Elliott, J. E. Barnes, F. Li, W. Tan, C. L. Cramer, P. Nandwana, M. Chmielus, Progress in Materials Science 2021, 119.

[11] H. Z. Ye, X. Y. Liu, H. P. Hong, Journal of Materials Processing Technology 2008, 200, 12.
[12] R. K. Enneti, S. J. Park, R. M. German, S. V. Atre, Materials and Manufacturing Processes 2012, 27, 103.
[13] E. M. Wilts, T. E. Long, Polymer International 2021, 70, 958.
[14] a) D. J. Hornbaker, R. Albert, I. Albert, A. L. Barabási, P. Schiffer, Nature 1997, 387, 765; b) M. Scheel, R. Seemann, M. Brinkmann, M. Di Michiel, A. Sheppard, B. Breidenbach, S. Herminghaus, Nature Materials 2008, 7, 189.
[15] M. Salehi, S. Maleksaeedi, M. L. S. Nai, M. Gupta, Additive Manufacturing 2019, 29.
[16] B. Derby, Annual Review of Materials Research 2010, 40, 395.
[17] S. M. Huang, R. X. Shen, B. Qian, L. Y. Li, W. H. Wang, G. H. Lin, X. F. Zhang, P. Li, Y. L. Xie, Journal of Physics D-Applied Physics 2018, 51.
[18] Z. G. Huang, Y. Tang, H. Guo, X. Y. Feng, T. T. Zhang, P. Li, B. Qian, Y. L. Xie, Ceramics International 2020, 46, 10096.
[19] S. Y. Tang, Y. R. Yang, Z. T. Fan, L. Yang, Z. Y. Yang, Q. Ling, P. L. Wang, Ceramics International 2022, 48, 7963.
[20] a) P. Innocenzi, L. Malfatti, S. Costacurta, T. Kidchob, M. Piccinini, A. Marcelli, The Journal of Physical Chemistry A 2008, 112, 6512; b) C. Liu, E. Bonaccurso, H.-J. Butt, Physical Chemistry Chemical Physics 2008, 10, 7150.
[21] M. Singh, H. M. Haverinen, P. Dhagat, G. E. Jabbour, Advanced Materials 2010, 22, 673.
[22] N. D. Parab, J. E. Barnes, C. Zhao, R. W. Cunningham, K. Fezzaa, A. D. Rollett, T. Sun, Scientific Reports 2019, 9, 2499.
[23] H. Kim, F. Boulogne, E. Um, I. Jacobi, E. Button, H. A. Stone, Physical Review Letters 2016, 116, 124501.
[24] a) A. Mostafaei, A. M. Elliott, J. E. Barnes, F. Li, W. Tan, C. L. Cramer, P. Nandwana, M. Chmielus, Progress in Materials Science 2021, 119, 100707; b) J.-W. Oh, S. Nahm, B. Kim, H. Choi, Korean J. Met. Mater. 2019, 57, 227.
[25] P. Bajaj, A. Hariharan, A. Kini, P. Kürnsteiner, D. Raabe, E. A. Jägle, Materials Science and Engineering: A 2020, 772, 138633.
[26] E. M. F. de Souza Silva, G. S. da Fonseca, E. A. Ferreira, Journal of Materials Research and Technology 2021, 15, 4317.
[27] T. Rahman, W. L. Ebert, J. E. Indacochea, Corrosion Engineering, Science and Technology 2018, 53, 226.
[28] P. Statham, Microscopy and Microanalysis 1998, 4, 210.
[29] a) L. Chen, W. Chen, Z. Fu, G. Ding, Z. Chen, D. Zhu, Advanced Engineering Materials 2023, 25, 2200641; b) N. Lecis, M. Mariani, R. Beltrami, L. Emanuelli, R. Casati, M. Vedani, A. Molinari, Materials Science and Engineering: A 2021, 828, 142108.
[30] H. J. Sung, T. K. Ha, S. Ahn, Y. W. Chang, Journal of Materials Processing Technology 2002, 130, 321.